

Dispersion encoded full range frequency domain optical coherence tomography

Bernd Hofer^{1,2}, Boris Považay¹,
Boris Hermann¹, Angelika Unterhuber¹,
Gerald Matz², and Wolfgang Drexler^{1*}

¹*Biomedical Imaging Group, School of Optometry and Vision Sciences, Cardiff University,
Maindy Road, Cardiff, CF24 LU, United Kingdom*

²*Institute of Communications and Radio-Frequency Engineering, Vienna University of
Technology, Gusshausstrasse 25/ 389, A-1040 Vienna, Austria*

drexlerw@cf.ac.uk

Abstract: We propose an iterative algorithm that exploits the dispersion mismatch between reference and sample arm in frequency-domain optical coherence tomography (FD-OCT) to effectively cancel complex conjugate mirror terms in individual A-scans and thereby generate full range tomograms. The resulting scheme, termed dispersion encoded full range (DEFER) OCT, allows distinguishing real structures from complex conjugate mirror artifacts. Even though DEFER-OCT has higher post-processing complexity than conventional FD-OCT, acquisition speed is not compromised since no additional A-scans need to be measured, thereby rendering this technique robust against phase fluctuations. The algorithm uses numerical dispersion compensation and exhibits similar resolution as standard processing. The residual leakage of mirror terms is further reduced by incorporating additional knowledge such as the power spectrum of the light source. The suppression ratio of mirror signals is more than 50 dB and thus comparable to complex FD-OCT techniques which use multiple A-scans.

© 2008 Optical Society of America

OCIS codes: (110.4500) Imaging systems : Optical coherence tomography; (170.4500) Medical optics and biotechnology : Optical coherence tomography; (300.6300) Spectroscopy : Fourier transforms; (100.3010) Image processing: Image reconstruction techniques; (100.3020) Image processing: Image reconstruction-restoration; (100.5070) Image processing: Phase retrieval;

References and links

1. M. Wojtkowski, A. Kowalczyk, R. Leitgeb, and A. F. Fercher, "Full range complex spectral optical coherence tomography technique in eye imaging," *Opt. Lett.* **27**, 1415–1417 (2002). <http://www.opticsinfobase.org/ol/abstract.cfm?URI=ol-27-16-1415>
2. R. A. Leitgeb, C. K. Hitzenberger, A. F. Fercher, and T. Bajraszewski, "Phase-shifting algorithm to achieve high-speed long-depth-range probing by frequency-domain optical coherence tomography," *Opt. Lett.* **28**, 2201–2203 (2003). <http://ol.osa.org/abstract.cfm?URI=ol-28-22-2201>
3. P. Targowski, M. Wojtkowski, A. Kowalczyk, T. Bajraszewski, M. Szkulmowski, and W. Gorczynska, "Complex spectral OCT in human eye imaging in vivo," *Opt. Commun.* **229**, 79–84 (2004). <http://dx.doi.org/doi:10.1016/j.optcom.2003.10.041>
4. P. Targowski, W. Gorczynska, M. Szkulmowski, M. Wojtkowski, and A. Kowalczyk, "Improved complex spectral domain OCT for in vivo eye imaging," *Opt. Commun.* **249**, 357–362 (2005). <http://dx.doi.org/doi:10.1016/j.optcom.2005.01.016>

5. J. Zhang, J. S. Nelson, and Z. P. Chen, "Removal of a mirror image and enhancement of the signal-to-noise ratio in Fourier-domain optical coherence tomography using an electro-optic phase modulator," *Opt. Lett.* **30**, 147–149 (2005). <http://www.opticsinfobase.org/ol/abstract.cfm?URI=ol-30-2-147>
6. E. Götzinger, M. Pircher, R. A. Leitgeb, and C. K. Hitzenberger, "High speed full range complex spectral domain optical coherence tomography," *Opt. Express* **13**, 583–594 (2005). <http://www.opticsinfobase.org/oe/abstract.cfm?URI=oe-13-2-583>
7. M. A. Choma, C. Yang, and J. A. Izatt, "Instantaneous quadrature low-coherence interferometry with 3x3 fiber-optic couplers," *Opt. Lett.* **28**, 2162–2164 (2003). <http://ol.osa.org/abstract.cfm?URI=ol-28-22-2162>
8. M. V. Sarunic, M. A. Choma, C. H. Yang, and J. A. Izatt, "Instantaneous complex conjugate resolved spectral domain and swept-source OCT using 3x3 fiber couplers," *Opt. Express* **13**, 957–967 (2005). <http://www.opticsinfobase.org/oe/abstract.cfm?URI=oe-13-3-957>
9. M. V. Sarunic, B. E. Applegate, and J. A. Izatt, "Real-time quadrature projection complex conjugate resolved Fourier domain optical coherence tomography," *Opt. Lett.* **31**, 2426–2428 (2006). <http://www.opticsinfobase.org/ol/abstract.cfm?URI=ol-31-16-2426>
10. Y. Yasuno, S. Makita, T. Endo, G. Aoki, M. Itoh, and T. Yatagai, "Simultaneous B-M-mode scanning method for real-time full-range Fourier domain optical coherence tomography," *Appl. Opt.* **45**, 1861–1865 (2006). <http://ao.osa.org/abstract.cfm?URI=ao-45-8-1861>
11. R. K. Wang, "In vivo full range complex Fourier domain optical coherence tomography," *Applied Physics Letters* **90**, 054 103 (2007). <http://link.aip.org/link/?APL/90/054103/1>
12. R. A. Leitgeb, R. Michaely, T. Lasser, and S. C. Sekhar, "Complex ambiguity-free Fourier domain optical coherence tomography through transverse scanning," *Opt. Lett.* **32**, 3453–3455 (2007). <http://ol.osa.org/abstract.cfm?URI=ol-32-23-3453>
13. B. Baumann, M. Pircher, E. Götzinger, and C. K. Hitzenberger, "Full range complex spectral domain optical coherence tomography without additional phase shifters," *Opt. Express* **15**, 13375–13387 (2007). <http://www.opticsexpress.org/abstract.cfm?URI=oe-15-20-13375>
14. Y. K. Tao, M. Zhao, and J. A. Izatt, "High-speed complex conjugate resolved retinal spectral domain optical coherence tomography using sinusoidal phase modulation," *Opt. Lett.* **32**, 2918–2920 (2007). <http://ol.osa.org/abstract.cfm?URI=ol-32-20-2918>
15. S. Makita, T. Fabritius, and Y. Yasuno, "Full-range, high-speed, high-resolution 1- ∞ m spectral-domain optical coherence tomography using BM-scan for volumetric imaging of the human posterior eye," *Opt. Express* **16**, 8406–8420 (2008). <http://www.opticsexpress.org/abstract.cfm?URI=oe-16-12-8406>
16. S. Yun, G. Tearney, J. de Boer, and B. Bouma, "Removing the depth-degeneracy in optical frequency domain imaging with frequency shifting," *Opt. Express* **12**, 4822–4828 (2004). <http://www.opticsinfobase.org/oe/abstract.cfm?URI=oe-12-20-4822>
17. A. M. Davis, M. A. Choma, and J. A. Izatt, "Heterodyne swept-source optical coherence tomography for complete complex conjugate ambiguity removal," *J. Biomed. Opt.* **10**, 064005–6 (2005). <http://link.aip.org/link/?JBO/10/064005/1>
18. A. H. Bachmann, R. A. Leitgeb, and T. Lasser, "Heterodyne Fourier domain optical coherence tomography for full range probing with high axial resolution," *Opt. Express* **14**, 1487–1496 (2006). <http://www.opticsinfobase.org/oe/abstract.cfm?URI=oe-14-4-1487>
19. A. H. Bachmann, R. Michaely, T. Lasser, and R. A. Leitgeb, "Dual beam heterodyne Fourier domain optical coherence tomography," *Opt. Express* **15**, 9254–9266 (2007). <http://www.opticsexpress.org/abstract.cfm?URI=oe-15-15-9254>
20. B. J. Vakoc, S. H. Yun, G. J. Tearney, and B. E. Bouma, "Elimination of depth degeneracy in optical frequency-domain imaging through polarization-based optical demodulation," *Opt. Lett.* **31**, 362–364 (2006). <http://www.opticsinfobase.org/ol/abstract.cfm?URI=ol-31-3-362>
21. B. Cense, N. A. Nassif, T. C. Chen, M. C. Pierce, S. H. Yun, B. H. Park, B. E. Bouma, G. J. Tearney, and J. F. de Boer, "Ultrahigh-resolution high-speed retinal imaging using spectral-domain optical coherence tomography," *Opt. Express* **12**, 2435–2447 (2004). <http://www.opticsinfobase.org/oe/abstract.cfm?URI=oe-12-11-2435>
22. D. L. Marks, A. L. Oldenburg, J. J. Reynolds, and S. A. Boppart, "Autofocus algorithm for dispersion correction in optical coherence tomography," *Appl. Opt.* **42**, 3038–3046 (2003). <http://www.opticsinfobase.org/ao/abstract.cfm?URI=ao-42-16-3038>
23. M. Wojtkowski, V. J. Srinivasan, T. H. Ko, J. G. Fujimoto, A. Kowalczyk, and J. S. Duker, "Ultrahigh-resolution, high-speed, Fourier domain optical coherence tomography and methods for dispersion compensation," *Opt. Express* **12**, 2404–2422 (2004). <http://www.opticsinfobase.org/oe/abstract.cfm?URI=oe-12-11-2404>
24. K. E. O'Hara and M. Hacker, "Method to suppress artifacts in frequency-domain optical coherence tomography," *US7330270* (2008).
25. J. A. Izatt and M. A. Choma, *Optical Coherence Tomography Technology and Applications* (Springer, 2008), Vol. XXIX, chap. 2, "Theory of Optical Coherence Tomography", pp. 47–72. <http://www.springer.com/medicine/radiology/book/978-3-540-77549-2?detailsPage=samplePages>
26. A. F. Fercher, C. K. Hitzenberger, M. Sticker, R. Zawadzki, B. Karamata, and T. Lasser, "Numerical dispersion compensation for partial coherence interferometry and optical coherence tomography," *Opt. Express* **9**, 610–615

- (2001). <http://www.opticsinfobase.org/oe/abstract.cfm?URI=oe-9-12-610>
27. M. Duarte, M. Davenport, M. Wakin, and R. Baraniuk, "Sparse Signal Detection from Incoherent Projections," in *Proc. Int. Conf. on Acoustics, Speech and Signal Processing (ICASSP)* **3**, III305–308 (2006). <http://dx.doi.org/doi:10.1109/ICASSP.2006.1660651>
 28. B. Povazay, B. Hofer, B. Hermann, A. Unterhuber, J. E. Morgan, C. Glittenberg, S. Binder, and W. Drexler, "Minimum distance mapping using three-dimensional optical coherence tomography for glaucoma diagnosis," *J. Biomed. Opt.* **12**, 041204 (2007). <http://link.aip.org/link/?JBO/12/041204/1>
 29. E. J. Fernández, A. Unterhuber, B. Povazay, B. Hermann, P. Artal, and W. Drexler, "Chromatic aberration correction of the human eye for retinal imaging in the near infrared," *Opt. Express* **14**, 6213–6225 (2006). <http://www.opticsexpress.org/abstract.cfm?URI=oe-14-13-6213>
 30. R. K. Wang and Z. Ma, "A practical approach to eliminate autocorrelation artefacts for volume-rate spectral domain optical coherence tomography," *Phys. Med. Biol.* **51**, 3231–3239 (2006). <http://www.iop.org/EJ/abstract/0031-9155/51/12/015/>
 31. N. A. Nassif, B. Cense, B. H. Park, M. C. Pierce, S. H. Yun, B. E. Bouma, G. J. Tearney, T. C. Chen, and J. F. de Boer, "In vivo high-resolution video-rate spectral-domain optical coherence tomography of the human retina and optic nerve," *Opt. Express* **12**, 367–376 (2004). <http://www.opticsinfobase.org/oe/abstract.cfm?URI=oe-12-3-367>
 32. C. Dorrer, N. Belabas, J.-P. Likforman, and M. Joffre, "Spectral resolution and sampling issues in Fourier-transform spectral interferometry," *J. Opt. Soc. Am. B* **17**, 1795–1802 (2000). <http://www.opticsinfobase.org/josab/abstract.cfm?URI=josab-17-10-1795>
 33. M. Wojtkowski, R. Leitgeb, A. Kowalczyk, T. Bajraszewski, and A. F. Fercher, "In vivo human retinal imaging by Fourier domain optical coherence tomography," *J. Biomed. Opt.* **7**, 457–463 (2002). <http://dx.doi.org/10.1117/1.1482379>
 34. M. A. Choma, M. V. Sarunic, C. H. Yang, and J. A. Izatt, "Sensitivity advantage of swept source and Fourier domain optical coherence tomography," *Opt. Express* **11**, 2183–2189 (2003). <http://www.opticsinfobase.org/oe/abstract.cfm?URI=oe-11-18-2183>
 35. B. H. Park, M. C. Pierce, B. Cense, S. H. Yun, M. Mujat, G. J. Tearney, B. E. Bouma, and J. F. de Boer, "Real-time fiber-based multi-functional spectral-domain optical coherence tomography at 1.3 μm ," *Opt. Express* **13**, 3931–3944 (2005). <http://www.opticsinfobase.org/oe/abstract.cfm?URI=oe-13-11-3931>
 36. R. A. Leitgeb, W. Drexler, A. Unterhuber, B. Hermann, T. Bajraszewski, T. Le, A. Stingl, and A. F. Fercher, "Ultrahigh resolution Fourier domain optical coherence tomography," *Opt. Express* **12**, 2156–2165 (2004). <http://www.opticsinfobase.org/oe/abstract.cfm?URI=oe-12-10-2156>
 37. Y. Yasuno, V. D. Madjarova, S. Makita, M. Akiba, A. Morosawa, C. Chong, T. Sakai, K. P. Chan, M. Itoh, and T. Yatagai, "Three-dimensional and high-speed swept-source optical coherence tomography for in vivo investigation of human anterior eye segments," *Opt. Express* **13**, 10652–10664 (2005). <http://www.opticsinfobase.org/oe/abstract.cfm?URI=oe-13-26-10652>
 38. M. Mujat, B. H. Park, B. Cense, T. C. Chen, and J. F. de Boer, "Autocalibration of spectral-domain optical coherence tomography spectrometers for in vivo quantitative retinal nerve fiber layer birefringence determination," *J. Biomed. Opt.* **12**, 041205 (2007). <http://link.aip.org/link/?JBO/12/041205/1>
 39. W. Drexler, U. Morgner, F. X. Kärtner, C. Pitris, S. A. Boppart, X. D. Li, E. P. Ippen, and J. G. Fujimoto, "In vivo ultrahigh-resolution optical coherence tomography," *Opt. Lett.* **24**, 1221–1223 (1999). <http://www.opticsinfobase.org/ol/abstract.cfm?URI=ol-24-17-1221>
 40. J. F. de Boer, C. E. Saxer, and J. S. Nelson, "Stable carrier generation and phase-resolved digital data processing in optical coherence tomography," *Appl. Opt.* **40**, 5787–5790 (2001). <http://www.opticsinfobase.org/ao/abstract.cfm?URI=ao-40-31-5787>
 41. D. L. Marks, A. L. Oldenburg, J. J. Reynolds, and S. A. Boppart, "Digital algorithm for dispersion correction in optical coherence tomography for homogeneous and stratified media," *Appl. Opt.* **42**, 204–217 (2003). <http://www.opticsinfobase.org/ao/abstract.cfm?URI=ao-42-2-204>
 42. A. R. Tumlinson, B. Hofer, A. M. Winkler, B. Povazay, W. Drexler, and J. K. Barton, "Inherent homogenous media dispersion compensation in frequency domain optical coherence tomography by accurate k-sampling," *Appl. Opt.* **47**, 687–693 (2008). <http://ao.osa.org/abstract.cfm?URI=ao-47-5-687>
 43. Y. Yasuno, Y. Hong, S. Makita, M. Yamanari, M. Akiba, M. Miura, and T. Yatagai, "In vivo high-contrast imaging of deep posterior eye by 1- μm swept source optical coherence tomography andscattering optical coherence angiography," *Opt. Express* **15**, 6121–6139 (2007). <http://www.opticsexpress.org/abstract.cfm?URI=oe-15-10-6121>

1. Introduction

With standard frequency-domain optical coherence tomography (FD-OCT), only half of the available depth range is used due to the occurrence of so-called complex conjugate artifacts. The complex conjugate artifacts or mirrored signal components are caused by the symmetry

properties of the Fourier transform of a real-valued spectrum. Essentially the negative depth range (-range) is equal to the positive range (+range), if the dispersion of the interferometer sample and reference arm is properly matched in the optical system, thereby leading to symmetries around the zero-delay position. The +range is normally truncated in the final tomograms but components outside the -range fold back into the tomogram and cannot be distinguished from actual structures. Hence objects are imaged in the +range, away from the zero-delay, where the sensitivity would be the highest.

Complex FD-OCT techniques have been developed to allow use of the full depth range. They measure the complex spectrum by stepping the reference mirror [1–4], employing electro-optic phase modulators [5,6], using 3x3 fibre couplers [7–9], enforcing a sequential phase shift between consecutive A-lines [10–15] or frequency shifting [16–19] and polarization diversity [20]. Each technique has its advantages and disadvantages regarding complexity and quality. Common to all the techniques so far is the requirement of at least two measurements in order to reconstruct the full imaging range, therefore either increasing system complexity or reducing acquisition speed and transversal scanning range.

Dispersion mismatch between the two interferometer pathways leads to blurring of structures in the tomogram. Satisfactory compensation of physical dispersion mismatch can be achieved numerically as reported in [21–23]. While the peaks corresponding to true signal components will become narrower, mirrored signal components are further blurred as a side effect of numeric dispersion compensation [24]. This effect allows further suppression of residual mirrored signal components in complex FD-OCT [15]. Numerical dispersion compensation is also applied to the retinal tomograms in this paper by multiplying the measurements with a counter-dispersive complex phase term prior to inverse Fourier transformation.

In this manuscript, we propose to exploit the blurring effect by numeric dispersion compensation to reconstruct the full-range image. To this end, we consider the dispersion mismatch to actually encode the spectral phase and thereby position of individual complex signal components within the +range or -range. The resulting dispersion encoded full range (DEFRR) algorithm decodes the position and strength of true structures via an iterative procedure that requires only the actual dispersive phase as prior knowledge. Based on a simple physical model, we provide an intuitive implementation and block diagram for DEFRR, describing in detail the additionally required signal processing tasks. We show that reconstruction of the full image range from single measurements is possible using a novel scheme and test the algorithm on signals from a simple free-space interferometer. We also demonstrate the applicability to *in vivo* retinal imaging. In contrast to complex FD-OCT techniques that use more complicated measurement setups, DEFRR uses standard signal acquisition and shifts the complexity increase to post-processing. This suggests that our approach is well suited for ultra-high resolution OCT imaging.

2. Background and theory

2.1. OCT signal with dispersion

According to [23], let $S(\omega) = \bar{S}(\omega) + \tilde{S}(\omega)$ be the detected spectrum dependent on optical frequency ω . The background signal $\bar{S}(\omega) = |E_r(\omega)|^2 + |E_s(\omega)|^2$ and the interference signal $\tilde{S}(\omega) = 2\Re\{E_r^*(\omega)E_s(\omega)\}$ both depend on the time averaged electric fields $E_r(\omega)$ and $E_s(\omega)$ of the reference and sample arm, respectively. To evaluate the influence of bulk chromatic dispersion mismatch between E_r and E_s on $\tilde{S}(\omega)$ we consider a free-space Michelson interferometer (FSI) with a dispersion free reference arm of length z_r . The sample arm consists of multiple reflecting layers at geometrical positions $z_s^{(n)}$ that are embedded in dispersive material which starts at position z_d and has refraction index $n(\omega)$. The beam splitter surface is positioned at

depth $z = 0$ as in [25]. With this model the plane waves E_r and E_s can be written as

$$E_r(\omega) = \sqrt{I_r(\omega)} \exp\left(j\omega \frac{2z_r}{c_0}\right) \quad (1)$$

and

$$E_s(\omega) = \sum_n \sqrt{I_s^{(n)}(\omega)} \exp\left(j\omega \frac{2z_d}{c_0}\right) \exp\left(j\omega n(\omega) \frac{2(z_s^{(n)} - z_d)}{c_0}\right). \quad (2)$$

The splitting ratio of the beam splitter, power spectrum of the light source, polarization effects and detector efficiency are incorporated in the frequency dependent intensities $I_r(\omega)$ and $I_s^{(n)}(\omega)$ which also account for the individual reflectivities. Assuming a thin sample we can make the approximation $z_s^{(n)} - z_d \approx z_s^{(1)} - z_d = d$. This assumption very well applies to retinal imaging, corresponding to the dispersive vitreous of the eye of thickness d which is followed by the relatively thin retina comprised by layered structures [23]. Furthermore using the dispersion relation $k(\omega) = n(\omega)\omega/c_0$, (2) can be rewritten as

$$E_s(\omega) \cong \sum_n \sqrt{I_s^{(n)}(\omega)} \exp\left(j\omega \frac{2(z_s^{(n)} - d)}{c_0}\right) \exp\left(jk(\omega)2d\right), \quad (3)$$

and the interference signal is then given by

$$\tilde{S}(\omega) = 2 \sum_n \Re \left\{ \sqrt{I_r(\omega)I_s^{(n)}(\omega)} \exp\left(j\omega \frac{2(z_s^{(n)} - z_r)}{c_0}\right) \exp\left(j\left(k(\omega) - \frac{\omega}{c_0}\right)2d\right) \right\}. \quad (4)$$

The Taylor series expansion of $k(\omega)$ around the center frequency ω_0 , which reads [26]

$$k(\omega) = \sum_{i=0}^{\infty} a_i (\omega - \omega_0)^i, \quad a_i = \frac{1}{i!} \left. \frac{d^i k(\omega)}{d\omega^i} \right|_{\omega_0}, \quad (5)$$

can be used to identify the dispersion related phase distortion of $\tilde{S}(\omega)$ as

$$\exp(j\phi(\omega)) = \exp\left(j \sum_{i=2}^{\infty} \bar{a}_i (\omega - \omega_0)^i\right), \quad (6)$$

with the dispersion coefficients $\bar{a}_i = 2da_i$. Using (6), the reference position in the dispersive system $\tilde{z}_r = z_r + (1 - a_1 c_0)d$ and the dispersion shifted intensity $I^{(n)}(\omega) = 2\sqrt{I_r(\omega)I_s^{(n)}(\omega)} \exp\left(j\left(k(\omega_0) - a_1 \omega_0\right)2d\right)$ in (4), we obtain the interference signal

$$\tilde{S}(\omega) = \sum_n \Re \left\{ I^{(n)}(\omega) \exp\left(j\omega \frac{2(z_s^{(n)} - \tilde{z}_r)}{c_0}\right) \exp\left(j\phi(\omega)\right) \right\}. \quad (7)$$

With the optical delays $\tau_n = \frac{2(z_s^{(n)} - \tilde{z}_r)}{c_0}$ this finally results in the dispersed interference signal

$$\tilde{S}(\omega) = \sum_n I^{(n)}(\omega) e^{j\omega\tau_n} e^{j\phi(\omega)} + \sum_n I^{(n)*}(\omega) e^{-j\omega\tau_n} e^{-j\phi(\omega)}. \quad (8)$$

Dispersion compensation can be achieved by multiplying (8) with a compensating phase term $e^{-j\phi(\omega)}$. Thus we obtain the dispersion compensated signal

$$\tilde{S}_c(\omega) = \tilde{S}(\omega) e^{-j\phi(\omega)} = \underbrace{\sum_n I^{(n)}(\omega) e^{j\omega\tau_n}}_{\tilde{S}_d(\omega)} + \underbrace{\sum_n I^{(n)*}(\omega) e^{-j\omega\tau_n} e^{-j2\phi(\omega)}}_{\tilde{S}_m(\omega)}, \quad (9)$$

which is a superposition of the desired full range signal $\tilde{S}_d(\omega)$ and its ‘‘doubly–dispersed’’ conjugate mirror components $\tilde{S}_m(\omega)$.

2.2. DEFR algorithm

Our goal is to reconstruct $\tilde{S}_d(\omega)$ from a single measurement $\tilde{S}(\omega)$ and a given bulk dispersion $e^{j\phi(\omega)}$ based on the model derived above. To this end, we develop a signal model corresponding to the physical model presented in the preceding paragraph. This signal model is related to a model proposed in [27], which will allow us to propose a reconstruction algorithm based on a modified version of the algorithm used in [27].

Let $\mathbf{d} \in \mathbb{C}^N$ be the complex vector corresponding to the sampled desired full range signal $\tilde{S}_d(\omega)$ in (9), with sample points uniformly spaced in optical frequency ω . This signal can be reasonably modeled as a linear combination of $K < N$ vectors from the Fourier basis matrix $\Psi := [\boldsymbol{\psi}_1, \boldsymbol{\psi}_2, \dots, \boldsymbol{\psi}_N] \in \mathbb{C}^{N \times N}$, i.e.,

$$\mathbf{d} = \sum_{l=1}^K t_{n_l} \boldsymbol{\psi}_{n_l} = \Psi \mathbf{t}. \quad (10)$$

Here, the length- N vector \mathbf{t} has only K non-zero elements t_{n_l} , i.e., \mathbf{t} is a *sparse* vector. The parameter K is in the order of the number of reflecting layers from the physical model above, since with FD-OCT data the Fourier transform of the intensities $I^{(n)}(\omega)$ is usually very narrow.

Employing an $N \times N$ measurement matrix Φ , a measurement vector $\mathbf{f} \in \mathbb{R}^N$ that corresponds to uniform samples of the interference signal $\tilde{S}(\omega)$ can be calculated as

$$\mathbf{f} = \Phi \mathbf{d} + \Phi^* \mathbf{d}^* + \mathbf{w}, \quad (11)$$

where \mathbf{w} models measurement noise which will be considered in the discussion of Section 4. This is consistent with our physical OCT model in (8) when choosing $\Phi = \text{diag}(\boldsymbol{\phi})$ with $\boldsymbol{\phi} \in \mathbb{C}^N$ corresponding to uniform samples of the bulk dispersive phase $e^{j\phi(\omega)}$. By inserting (10) into (11) we obtain

$$\mathbf{f} = 2\Re\{\Phi \Psi \mathbf{t}\} + \mathbf{w}. \quad (12)$$

Our goal is to recover the sparse vector \mathbf{t} from the measured interference signal \mathbf{f} . It has been shown recently that problems of this kind can be phrased as ℓ_1 optimization, i.e. (cf. [27])

$$\hat{\mathbf{t}} = \underset{\mathbf{t}}{\text{argmin}} \|\mathbf{t}\|_1 \quad \text{subject to} \quad \Re\{\mathbf{V} \mathbf{t}\} = \mathbf{f}. \quad (13)$$

Here, $\|\mathbf{t}\|_1 = \sum_{n=1}^N |t_n|$ and $\mathbf{V} = 2\Phi \Psi$ is the *dispersive* basis. Our proposed DEFR reconstruction searches for a sparse representation of the measurement vector \mathbf{f} in the dictionary $\{\mathbf{v}_i\}$ consisting of the column vectors of the dispersive basis \mathbf{V} (cf. [27]). To this end, we adapt the greedy matching pursuit (MP) algorithm proposed in [27] for the preceding signal model in order to iteratively find locally optimum solutions of (13). The algorithm requires specification of the maximum number $I \geq K$ of iterations and of the fraction ε of the energy of \mathbf{f} that may remain in the residual, which usually depends on the noise level and modeling errors (cf. [27]).

MP ALGORITHM FOR DEFR FD-OCT SIGNAL RECONSTRUCTION

1. Initialization: residual $\mathbf{r}_0 = \mathbf{f}$; approximation $\hat{\mathbf{t}} = \mathbf{0}$; iteration counter $i = 1$.
2. Determine the dictionary vector which is maximally collinear with the residual,

$$n_i = \arg \max_{n=1 \dots N} |c_{i,n}|, \quad \text{with} \quad c_{i,n} = \frac{\langle \mathbf{v}_n, \mathbf{r}_{i-1} \rangle}{\|\mathbf{v}_n\|}. \quad (14)$$

3. Update the estimate of the corresponding signal component and the residual:

$$\hat{\mathbf{t}}_{n_i} = \hat{\mathbf{t}}_{n_i} + 2c_{i,n_i}, \quad (15)$$

$$\mathbf{r}_i = \mathbf{r}_{i-1} - 2\Re \left\{ c_{i,n_i} \frac{\mathbf{v}_{n_i}}{\|\mathbf{v}_{n_i}\|} \right\} = \mathbf{r}_{i-1} - c_{i,n_i} \frac{\mathbf{v}_{n_i}}{\|\mathbf{v}_{n_i}\|} - c_{i,n_i}^* \frac{\mathbf{v}_{n_i}^*}{\|\mathbf{v}_{n_i}\|}. \quad (16)$$

4. Increment i . If $i < I$ and $\|\mathbf{r}_i\|^2 > \varepsilon \|\mathbf{f}\|^2$, then continue iterating with Step 2; otherwise proceed with Step 5.

5. Obtain the estimate for the desired full range complex FD-OCT signal:

$$\hat{\mathbf{d}} = \Psi \hat{\mathbf{t}}. \quad (17)$$

We note that the factor of 2 in (16) and (15) is required to preserve signal energy.

3. Methods

3.1. Experimental setup

For *in vivo* imaging an ophthalmic FD-OCT system operating at 800 nm was used, which employed a 90/10 fiber-based interferometer interfaced to a fundus camera and a spectrometer [28]. The light source was a broadband Ti:sapphire laser (140 nm full width half maximum (FWHM)) at 800 nm (FEMTOLASER, Integral). The detection system utilized a 2048 pixel silicon CCD-camera (AVIIVA, Atmel M2 CL2014-BAO) based spectrometer and imaging was performed at a line rate of 20 kHz. Residual dispersion of the system and of the eye's vitreous, which is equivalent to ~ 25 mm of water, was not compensated. However, polarization mismatch between the two arms was corrected by fiber-optic polarization paddles in both arms and optimized for wide spectral throughput. The optical power at the cornea did not exceed $800 \mu\text{W}$ when imaging normal subjects at the fovea in a typical 8° (2.3 mm) wide horizontal scan. Scans were performed at different zero delay positions. Strongest overlapping of complex conjugate artifacts was found when setting the zero delay position in the middle of the retina at the outer nuclear layer, around 150-200 μm optical path length away from the retinal surface. The real time preview image was numerically corrected online for dispersion, which permitted to adjust the focus and to align the subject for position and tilt.

To calibrate the spectrometer and test the proposed scheme, a simple Michelson-type free-space interferometer (FSI) was set up and interfaced to the light source and the spectrometer. Based on a non-polarizing 50/50 prism-cube beam splitter and a reference arm, mounted on a translation-stage with fiber-optic input and output collimators the device permitted to balance power in both arms by a reflective continuous neutral density filter wheel.

To test the algorithms dependency on the amount of dispersion mismatch, different dispersive materials were alternatively inserted into the sample arm of the free space interferometer. A 25 mm deep glass-cuvette filled with water ("H₂O 25 mm"); an 8 mm thick achromatic triplet ("Achromatizer") consisting of two materials, 3 mm F2 and 5 mm N-SK4, used for axial chromatic aberration correction of the human eye [29]; two BK7 1 mm microscope slides ("Glass 2 mm") and a single BK7 1 mm microscope slide ("Glass 1 mm") were used. The optical delay was compensated for by adjusting the reference mirror position accordingly and the intensity across the full spectral bandwidth was set to be flat with a similar quasi-Gaussian spectral profile. Due to the simple free-space setup the polarization difference between both arms was negligible.

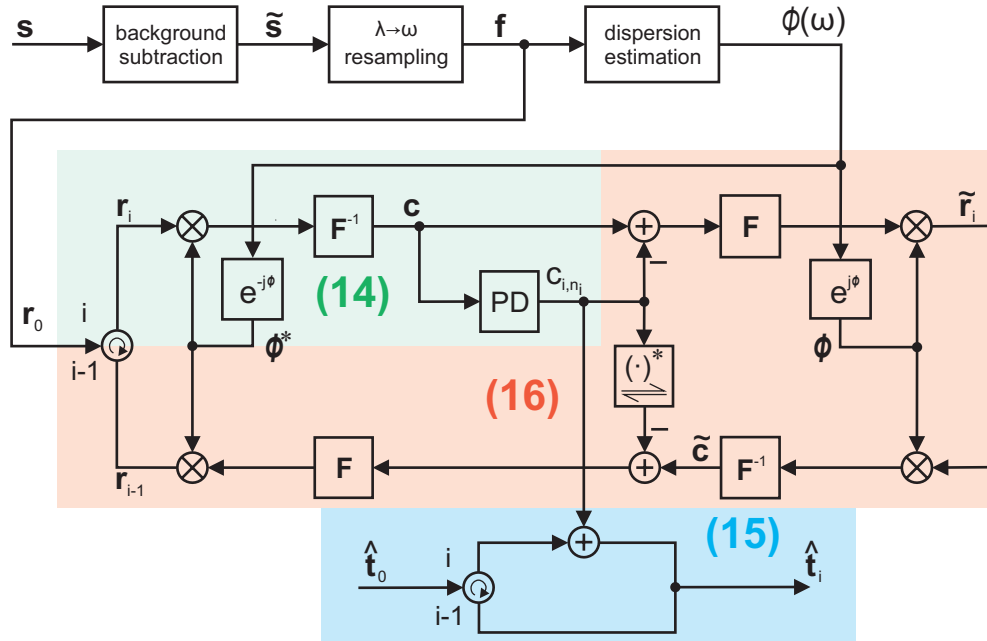


Fig. 1. Block diagram of the dispersion encoded full range (DEFRR) algorithm and associated pre-processing steps. The iterative procedure is indicated by iteration index i . The peak detector is denoted as **PD**; further notations: measured raw signal \mathbf{s} , interference signal $\tilde{\mathbf{s}}$, measurement vector \mathbf{f} , dispersive phase term $\phi(\omega)$ and corresponding vector $\boldsymbol{\phi}$, fast Fourier transform \mathbf{F} , residual signal \mathbf{r} , intermediate spatial signal \mathbf{c} ; and finally the complex full range tomogram line $\hat{\mathbf{t}} \in \mathbb{C}^N$. The diagram parts associated with equations (14), (16) and (15) are high-lighted in green, red and blue, respectively.

3.2. Signal processing

Figure 1 shows the block diagram for the proposed algorithm. Also the associated pre-processing steps are included. Data from both experimental setups were treated in almost the same manner, differences will be indicated where applicable. Let $\mathbf{s} \in \mathbb{R}^N$ be the measured raw signal corresponding to the non-uniformly sampled detected spectrum $S(\omega_p)$ with sample frequencies ω_p . Autocorrelation terms and fixed pattern noise are removed from \mathbf{s} via background subtraction. The resulting corrected spectrum $\tilde{\mathbf{s}} \in \mathbb{R}^N$ corresponds to the sampled interference signal $\tilde{S}(\omega_p)$. The measurement vector \mathbf{f} whose elements correspond to uniform samples of $\tilde{S}(\omega)$ is then obtained via resampling of $\tilde{\mathbf{s}}$. The sample frequencies ω_p depend on the pixel indices $p \in \{1, \dots, N\}$ of the CCD linescan camera employed in the spectrometer (in our setup, $N = 2048$). Specifically, the frequencies ω_p correspond to approximately uniformly spaced samples in the wavelength domain, i.e., $\omega \propto \lambda^{-1}$. We describe below how to determine the actual mapping $\omega_p = g(p)$. In addition to \mathbf{f} , the DEFRR algorithm as shown in Fig. 1 requires the vector $\boldsymbol{\phi}$ of uniform samples of the frequency-dependent dispersive phase term $e^{j\phi(\omega)}$ as input. The estimation of $\boldsymbol{\phi}$ from \mathbf{f} will be discussed below. The output of the algorithm consists of a complex full range tomogram line $\hat{\mathbf{t}} \in \mathbb{C}^N$.

3.3. DEFRR algorithm implementation

Next we explain the implementation of the DEFRR algorithm introduced in Section 2 in more detail, which essentially corresponds to the lower portion of the block diagram in Fig. 1. The preprocessing steps, background subtraction, resampling and dispersion estimation, will then

be described in some detail in the remainder of this section. The initial residual signal \mathbf{r}_0 equals the background-corrected and resampled interference spectrum \mathbf{f} , whereas the initial output signal $\hat{\mathbf{t}}_0$ is the all-zero vector. First, numeric dispersion compensation is performed by element-wise multiplication of the residual with the phase vector ϕ^* and then the signal in the spatial domain is calculated via an inverse fast Fourier transform (FFT), denoted by the matrix \mathbf{F} . This corresponds to the calculation of the intermediate spatial signal $\mathbf{c}_i = (c_{i,1} \dots c_{i,N})^T$ containing all N normalized inner products $c_{i,n} = \langle \mathbf{v}_n, \mathbf{r}_{i-1} \rangle / \|\mathbf{v}_n\|$, $n = 1, \dots, N$ in (14). A peak detector finds the position n_i and complex coefficient $c_{i,n_i} = \langle \mathbf{v}_{n_i}, \mathbf{r}_{i-1} \rangle / \|\mathbf{v}_{n_i}\|$ of the strongest signal component. Thereby, the peak detector is simply looking for the position of the element of $|\mathbf{c}_i|$ with maximum value. The output signal $\hat{\mathbf{t}}_i$ at position n_i is then updated with c_{i,n_i} according to (15).

What follows is the determination of the update of the residual (cf. (16)). To this end, the signal component c_{i,n_i} is subtracted from the intermediate spatial domain signal \mathbf{c}_i , which then undergoes FFT and inverse dispersion compensation. This amounts to removing the true signal component in the spectral domain. To cancel mirror artifacts (corresponding to the complex conjugate term in the right-hand side of (16)), the inverse dispersive phase is applied again and another inverse FFT provides an intermediate spatial domain signal $\tilde{\mathbf{c}}_i$. The complex conjugate of the true signal component c_{i,n_i} is then subtracted from $\tilde{\mathbf{c}}_i$ at the mirror position $|N - n_i|$. Finally, computing the FFT of the ‘‘cleaned’’ intermediate spatial domain signal and undoing the inverse dispersion yields the new residual signal \mathbf{r}_i . This procedure continues in an iterative manner, adding further signal components to the output signal $\hat{\mathbf{t}}$ until the residual signal contains only noise, i.e., $\|\mathbf{r}_i\|^2 < \varepsilon \|\mathbf{f}\|^2$, or a maximum number of iterations I is reached.

3.4. Background subtraction

Let $\mathbf{b} \in \mathbb{R}^N$ be the background signal corresponding to the non-uniformly sampled background spectrum $\bar{S}(\omega_p)$. To determine \mathbf{b} , we employ two different strategies:

- For *in vivo* imaging we obtain \mathbf{b} as the mean value of the detected signals $\mathbf{s}_x, x = 1, \dots, N_x$, from a whole tomogram, i.e., $\mathbf{b} = \frac{1}{N_x} \sum_{x=1}^{N_x} \mathbf{s}_x$ (here, x is a spatial index determining the transversal position of an A-scan on the tomogram consisting of $N_x = 1024$ lines). This is reasonable when imaging biological samples, since their interference spectra $\tilde{S}_x(\omega_p)$ will average out over a suitable transversal scan range due to structural independence and phase fluctuations [30].
- For artificial samples such as the translation stage experiment, we determine \mathbf{b} as a linear combination $\mathbf{b} = \mathbf{b}_s + \mathbf{b}_r - \mathbf{b}_d$. Here, \mathbf{b}_s is the background signal from the sample arm when the reference arm is blocked, \mathbf{b}_r is the background signal from the reference arm with blocked sample arm, and \mathbf{b}_d is the dark background signal due to a fixed pattern offset on the CCD when both interferometer arms are blocked. To reduce the influence of measurement noise all signals are averaged over $N_x = 1024$ sequential measurements.

Different background correction strategies have been previously described for FD-OCT. Multiplicative background suppression is proposed in [31] and background subtraction is briefly described in [23] and in more detail in [30]. In our system, the strength of the background signal fluctuates over successive tomogram lines, which is probably caused by timing issues within the CCD-electronics of the employed camera. We therefore use a subtractive background correction that *additionally* adjusts for the strength of the background signal via the normalized inner product $\langle \mathbf{b}, \mathbf{s} \rangle / \|\mathbf{b}\|^2$, i.e.,

$$\tilde{\mathbf{s}} = \mathbf{s} - \frac{\langle \mathbf{b}, \mathbf{s} \rangle}{\|\mathbf{b}\|^2} \mathbf{b}. \quad (18)$$

This procedure effectively suppresses shaded horizontal lines otherwise visible on *in vivo* tomograms.

3.5. Spectrometer calibration and resampling

Exact calibration of the spectrometer sampling points ω_p is essential for achieving depth independent high resolution in the spatial domain as has been shown in [32]. A parametric approach is to choose $\omega_p \propto p^{-1}$ [33,34] as a first approximation that can be improved by taking the grating equation into account [31,35]. Non-parametric approaches aim to use calibration targets within an interferometric setup. Here, ω_p is estimated by local phase analysis of the spectral data from single reflections [36–38]. To account for the entanglement with the phase induced by residual dispersion mismatch, a second measurement at different optical path length difference (OPD) can be used [15]. The non-parametric approaches are especially suited for systems employing broad-band lasers since each pixel can in principle be characterized individually as opposed to calibration light sources which only provide a limited number of spectral reference lines. Slight deviations from the true ω_p will lead to depth dependent resolution loss. Thus, we use a phase analysis based calibration procedure as follows.

The input fiber of the spectrometer is connected to the FSI. The calibration of ω_p remains mechanically long-term stable (> 6 months) as long as the most critical component, the input fiber, stayed connected to the FC/APC connector on the collimator of the spectrometer. The FSI was adjusted such that virtually no dispersion mismatch between both interferometer arms occurred, which was verified during the phase analysis. Recordings for several OPDs were taken and according to (7) the spectrometer output interference signal from the simple free space setup with $I(\omega_p) \in \mathbb{R}$ then reads

$$\tilde{S}(\omega_p) = I(\omega_p) \Re \left\{ \exp \left(j\omega_p \frac{2(z_s - z_r)}{c_0} \right) \right\} = I(\omega_p) \Re \{ \exp(j\omega_p \tau_z) \}. \quad (19)$$

The position-dependent phase $\varphi_{p,z} = \omega_p \tau_z$ can thus be obtained as the phase of the analytic signal of (19). For known positions τ_z the mapping function $g(p) = \omega_p$ can be derived from $\varphi_{p,z}$ and used for resampling onto the uniform grid

$$\omega_u = \omega_1 + \frac{\omega_N - \omega_1}{N-1} \left(u + \frac{N}{2} \right), \quad \omega_u \in [\omega_1, \omega_N], \quad (20)$$

with $u = \left[-\frac{N}{2}, \dots, \frac{N}{2} - 1 \right]$ being a discrete frequency index that is related to the pixel index p via $u = p - \frac{N}{2}$. To render the exact position τ_z onto the determination of the ω_p from $\varphi_{p,z}$ we recast the mapping function $g(p)$ by employing a *discrete mapping function* $\tilde{g}(u) \in \left[-\frac{N}{2}, \frac{N}{2} - 1 \right]$. To this end the sampling frequencies ω_p are expressed as a polynomial function in u , which reads

$$\omega_{p(u)} = b_0 + b_1 u + b_2 u^2 + b_3 u^3 + \dots = b_0 + b_1 u + \tilde{\omega}_{p(u)}. \quad (21)$$

Thereby b_0 and b_1 are readily determined as $b_0 = \omega_1 + \frac{N}{2} b_1$, $b_1 = \frac{\omega_N - \omega_1}{N-1}$ and the higher order terms have been combined into $\tilde{\omega}_{p(u)}$. The mapping function $g(p)$ can now be rewritten from (21) by using the discrete mapping function $\tilde{g}(u)$, i.e.,

$$g(p) = \omega_{p(u)} = \omega_1 + \frac{\omega_N - \omega_1}{N-1} \left(\tilde{g}(u) + \frac{N}{2} \right), \quad \text{with } \tilde{g}(u) = u + \frac{\tilde{\omega}_{p(u)}}{b_1}. \quad (22)$$

From Eqs. (20) and (22) we observe that resampling from ω_p to ω_u corresponds to resampling from $\tilde{g}(u)$ to u . Given the phase function $\varphi_{p,z} = \omega_{p(u)} \tau_z = b_0 \tau_z + b_1 \tau_z u + \tilde{\omega}_{p(u)} \tau_z$ we can calculate $\tilde{g}(u)$ as $\tilde{g}(u) = \frac{\varphi_{p,z} - b_0 \tau_z}{b_1 \tau_z}$. If the discrete mapping function $\tilde{g}(u)$ is used for resampling, the

position τ_z does not need to be known exactly. Only the combined terms $b_0\tau_z$ and $b_1\tau_z$ have to be estimated and can finally be obtained directly from $\varphi_{p,z}$ via least-squares estimation:

$$\begin{bmatrix} b_0\tau_z \\ b_1\tau_z \end{bmatrix} = \left([\mathbf{1} \ \mathbf{u}]^T [\mathbf{1} \ \mathbf{u}] \right)^{-1} [\mathbf{1} \ \mathbf{u}]^T \boldsymbol{\varphi}_z, \quad (23)$$

where $\mathbf{1} \in \mathbb{R}^N$, $\mathbf{u} = \left[-\frac{N}{2} \dots \frac{N}{2} - 1 \right]^T$ and $\boldsymbol{\varphi}_z \in \mathbb{R}^N$ with elements $\varphi_{p,z}$.

Any dispersion mismatch would be visible as separation of the non-linear phase functions $\tilde{g}(u) - u$ from positive and negative OPDs. Since the dispersion was closely matched this effect is not visible. Measurement noise is reduced by averaging 1024 sequentially measured values of the \tilde{s}_z corresponding to $\tilde{S}(\omega_p)$. Furthermore the accuracy of depth independence of the extracted mapping function $\tilde{g}(u)$ is increased by averaging over several positive and negative positions z . Only positions not effected by aliasing are considered, since the phase function is corrupted above 2/3 of the depth range due to aliasing around positive and negative end of depth (EOD). We also exclude positions close to the zero delay (ZD) position (within $\pm 50 \mu\text{m}$) for which an overlap with the complex conjugate terms occurs. Finally influence of an internal reflection from the light source can be reduced by band-pass filtering the main peak. We used linear resampling of the signals \tilde{s} from $\tilde{g}(u)$ to u . Up-sampling by a factor 2 and sinc-interpolation filter with length $2N$ was used prior to the resampling to prevent additional aliasing components close to EOD and to reduce resampling errors of the fast linear procedure. Finally the resampled signals were decimated again to obtain the measurements \mathbf{f} .

3.6. Dispersion compensation and estimation

A number of different approaches have been proposed for dispersion compensation and thus resolution enhancement for OCT. Proper dispersion management is essential when using broad bandwidth light sources and can be accomplished by hardware dispersion balancing of both interferometer arms [39]. Software dispersion compensation by application of a correcting phase term in the frequency domain was already proposed in [26, 40] and is well suited for FD-OCT [21, 23]. It was also recognized that phase adaptation can be realized via signal resampling [22, 41], which is also well applicable to swept-source FD-OCT [42]. As described above we implement dispersion compensation by applying the compensating phase term $e^{-j\phi(\omega)}$ prior to inverse FFT. We estimate the frequency-dependent dispersive phase $\phi(\omega)$ using information entropy of the spatial domain signal (on a linear scale) as sharpness metric $R(\cdot)$. This is equivalent to the procedure described in [43]. We only determine two parameters \hat{a}_2 and \hat{a}_3 corresponding to the second and third order dispersion coefficients \bar{a}_2 and \bar{a}_3 in (6), i.e., $\phi(\omega_u) = \frac{1}{N-1}(\hat{a}_2 u^2 + \hat{a}_3 u^3)$. This is sufficient in our measurements and results in nearly no deviation from the optimal free-space resolution as shown later. For data from the free-space interferometer we combined measurements at several OPDs to estimate dispersion from this combined OCT image and thereby ensured depth-independence of the estimated dispersion coefficients.

For measurements with dispersion mismatch by a 25 mm deep glass cuvette filled with water, the optimization procedure for the sharpness metric $R(\hat{a}_2, \hat{a}_3)$ (which here depends on the dispersion parameters \hat{a}_2 and \hat{a}_3) is illustrated in Fig. 2. For fixed $\hat{a}_3 = 0$, the sharpness metric is minimized by $\hat{a}_2 = -0.083$, yielding $R(-0.083, 0) = 5.6$ (cf. Fig. 2(a)). Now fixing $\hat{a}_2 = -0.083$, optimization with respect to \hat{a}_3 leads to $R(-0.083, -0.011) = 5.55$ (cf. Fig. 2(b)). Iteratively continuing this alternating optimization or jointly optimizing \hat{a}_2 and \hat{a}_3 via a 2-D grid search leads to the global minimum of 5.43 at $\hat{a}_2 = -0.089$ and $\hat{a}_3 = -0.025$ (cf. Fig. 2(c)).

In Fig. 2(d) it can be seen that prior to dispersion compensation the raw signals' magnitude from positive OPDs (solid lines) and mirror terms from negative OPDs (dashed lines) cannot be differentiated and are equally blurred. The dispersion compensated signals over the positive

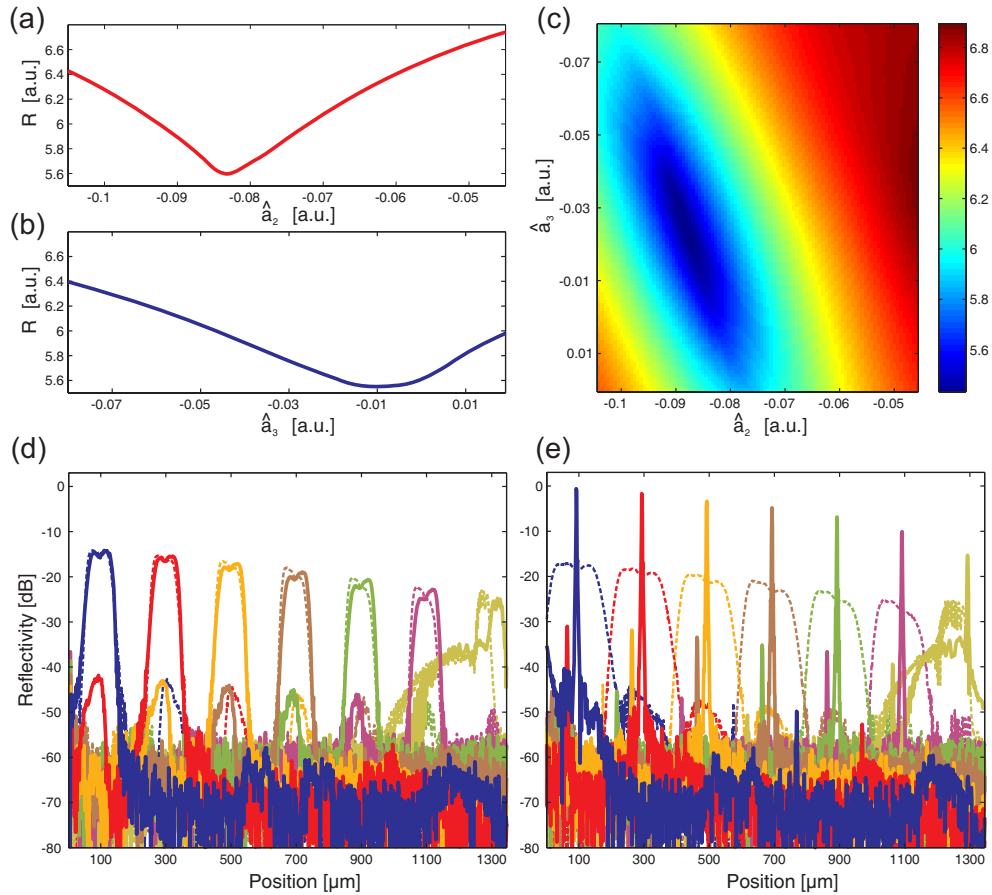


Fig. 2. (a) Sharpness metric R as a function of dispersion parameter \hat{a}_2 with $\hat{a}_3 = 0$, (b) R as function of \hat{a}_3 with $\hat{a}_2 = -0.083$, i.e., the optimum value from (a), (c) combined optimization of \hat{a}_2 and \hat{a}_3 to find the global sharpness optimum, (d) mirror signals for various positions, (e) mirror signals after application of compensation phase; positive positions are plotted as solid lines, signals from negative mirror positions as thin dashed lines.

depth range are shown in Fig. 2(e). Signals originating from the +range appear sharp, whereas the mirror terms in the -range are further blurred and can thus be clearly differentiated from the non-mirrored (true) signal components. This practically demonstrates the basis of the DEFR algorithm. Whereas here the mirror terms are 16 dB below the true signals, this separation is much lower for smaller dispersion mismatch (10 dB for “Achromatizer”, 5 dB “Glass 2mm”, 2.5 dB “Glass 1mm”).

4. Results and discussion

Fig. 3 depicts results for mirror signals with various optical path delays measured with the FSI using the same source and spectrometer as for *in vivo* imaging. The FWHM output bandwidth of the setup was determined as 120 nm. Dispersion mismatch was obtained by introducing a 25 mm water cell into the reference arm. Standard processing included dispersion compensation and calculation of the inverse FFT. Blurred mirror terms visible in Fig. 3(a) at positive positions are clearly cancelled by the DEFR algorithm (Fig. 3(b)). For the algorithm the number of iterations was set to the number of sample points $I = N = 2048$. The stopping parameter ϵ was set to 0 in all experiments, thus also the noise floor \mathbf{w} was reconstructed (cf. (11)) which

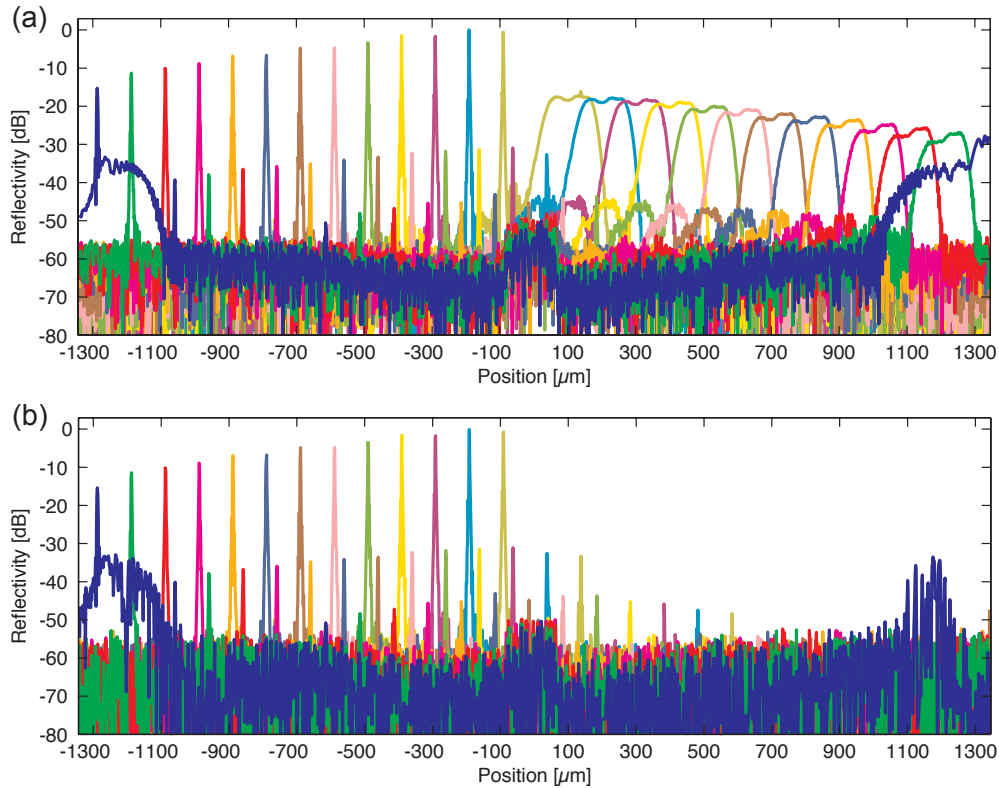


Fig. 3. (a) Mirror signals after dispersion compensation, (b) mirror signals after dispersion encoded full range (DEFR) algorithm. Signals at different positions are plotted using different colors.

also confirms the algorithms stability since the algorithm did not diverge after all signal components have been found. We note that the noise w in an OCT system is typically comprised of residual coherent noise terms which have not been removed by background subtraction and might also not necessarily fit into the dispersive signal model proposed in Section 2, furthermore it includes detector shot noise as well as electronic noise. Since no further knowledge about w was used in the derivation of the algorithm (cf. (13)), the ability of the algorithm to reconstruct the noise floor of the system experimentally verifies this necessary condition for stability after convergence.

The expected convergence behavior was verified by monitoring subsequent iterations: the algorithm first finds signal components above the noise floor; since it is not stopped it continues with noisy components. Internal reflections of the light source become visible -32 dB and -44 dB below the corresponding main peaks. Especially in the positive range these auxiliary peaks demonstrate the ability of the algorithm to reconstruct signals buried in the very strong blurred mirror terms, e.g. such as the peaks at 150 μm and 300 μm . The algorithm also behaves stably regarding aliased terms at EOD, which can be seen for the blue curve with its main peak at -1300 μm close to the EOD at 1320 μm . The aliased mirror terms are greatly reduced in the positive range. The remaining fragment at about 1200 μm probably originates from the next zero delay position. It also appears that autocorrelation terms are greatly reduced, e.g. the -45 dB side peak (brown line) becomes visible at ZD position. The stability of the algorithm was also tested by superposition of the raw signals for different positions. Thus it was confirmed that even equally strong peaks at the same absolute position can be resolved correctly.

Properties for DEFR reconstruction and influence of bandwidth and different dispersion lev-

els on the algorithm's performance were quantified and are shown in Fig. 4(a)-(c). To evaluate the influence of the dispersion level, different materials were inserted in the sample-arm of the free-space interferometer as described above. To verify the ability of the algorithm to perform well also on signals with standard resolution bandwidth, the raw signals were band-limited to a 55 nm FWHM Gaussian shaped spectrum. Since the bandwidth reduced signals have smaller power as compared to the full bandwidth signals, the 120 nm and 55 nm signal loss curves differ by about 7 dB. The drop in signal power for the 55 nm signals was compensated for determination of the suppression ratio to allow a direct comparison with respect to the different bandwidths and materials. Since the complex conjugate mirror terms after the DEFR algorithm were in the order of the noise components, the suppression ratio was the average value from 128 measurements. Following [12], the suppression ratio was defined as magnitude of the signal peak divided by the magnitude of the signal at the conjugate peak position.

The DEFR algorithm exhibits the same depth dependent signal loss as conventional processing (Fig. 4(a)), i.e., the curves for 120 nm standard processing (SP) (solid green) and DEFR algorithm (red squares) nearly overlap as well as the curves for 55 nm SP (dashed cyan) and DEFR (blue squares). It is also apparent that inserting no dispersive material resulted in the highest signal. The optical elements 1 mm glass, 2 mm glass and the achromatizer result in signal intensities reduced by only 1 dB, whereas with the 25 mm water cell a 3 dB signal reduction due to absorption is observed. This suggests that for applications in non-ophthalmic imaging, optical elements with less absorption should be employed to cause a dispersion mismatch usable for DEFR. However, for retinal imaging the vitreous of the eye causes a natural dispersion mismatch and the observed signal reduction would be inherent.

Since mirror terms are suppressed down to the noise level (cf. Fig. 3(b)), accordingly the artifact suppression ratio exhibits a value of more than 50 dB (Fig. 4(b)). As a first impression the curves appear very similar with a shape dominated by the signal loss, i.e., the suppression ratio decreases towards EOD. This demonstrates the ability of the algorithm to cope with less bandwidth (55 nm) and less dispersion mismatch (1 mm glass). As a trend the algorithm performs at 120 nm bandwidth slightly better than at 55 nm for the individual materials and more dispersion provides a higher suppression ratio. Not taking into account values above $\pm 1200 \mu\text{m}$, which are influenced by aliasing terms and signals from the subsequent ZDs, shows the expected behavior: the least dispersion mismatch and smallest bandwidth signal (1 mm glass, 55 nm) resulted in the weakest suppression ratio, high dispersion and high bandwidth provides best results (25 mm water cell, 120 nm) with a separation of around 7 dB. The result for the achromatizer and 120 nm slightly outperformed the 25 mm water cell. We believe this was due to the high asymmetric third order dispersion with this optical element, which suggests that materials or material combinations with increased higher order dispersion are interesting candidates to be used within the DEFR scheme. It has to be noted that broader bandwidth and higher dispersion mismatch results in more broadened complex conjugate artifacts of the standard processing Fig. 3(a). Thus the suppression ratio of the numeric dispersion compensation itself can be evaluated to be ~ 16 dB for the 25 mm water cell, ~ 10 dB for achromatizer, ~ 5 dB for 2 mm glass, and ~ 2.5 dB for 1 mm glass at 120 nm bandwidth. However, the algorithm aims to cancel the mirror terms rather than blurring them as can be seen from Fig. 3(b), increased dispersion thereby helps the algorithm to better confine the signal components from mirror terms.

Tomogram resolution (see Fig. 4(c)), exhibits similar values for different levels of dispersion. The theoretical axial resolution with a laser spectrally centered at 824 nm are 2.5 μm and 5.5 μm for 120 nm and 55 nm FWHM, respectively. The measured resolutions for a Gaussian shaped 55 nm signal are closer to the theoretical value than the 120 nm full bandwidth signals because the laser spectrum deviated from the theoretical Gaussian shape. As mentioned above, the depth-independence of the resolution indicates that our frequency resampling was

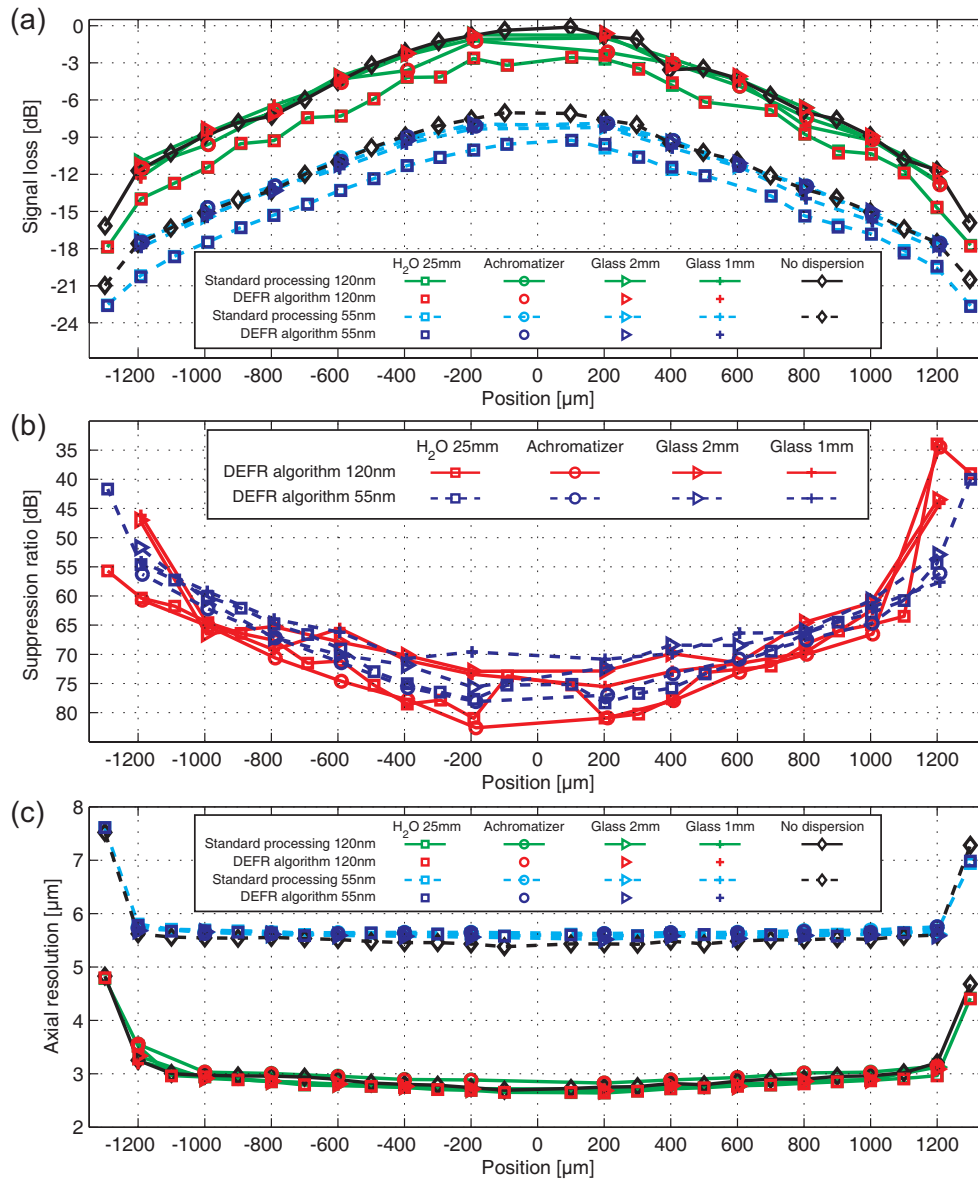


Fig. 4. (a) Signal loss after DEFR algorithm, (b) artifact suppression ratio of the DEFR algorithm, (c) resolution with no dispersion (black curve) and after dispersion compensation for different dispersive materials in sample arm. Results for 120 nm and 55 nm bandwidth are plotted as solid and dashed lines, respectively. Results for standard processing are plotted in green (120 nm) and cyan (55 nm), DEFR algorithm in red (120 nm) and blue (55 nm).

sufficiently accurate.

Results for *in vivo* imaging are depicted in Fig. 5. Dispersion compensation was applied to the standard FD-OCT images. The dispersion parameters were determined on the data set of Fig. 5(b) and used for all tomograms. As shown in Fig. 5(a)-(d), the blurred complex conjugate artifacts are clearly visible in the retinal tomograms after standard processing. The image without dispersion compensation features symmetries around the zero-delay position indicated by the yellow line. Typically, the +range is omitted in the final tomograms as indicated in

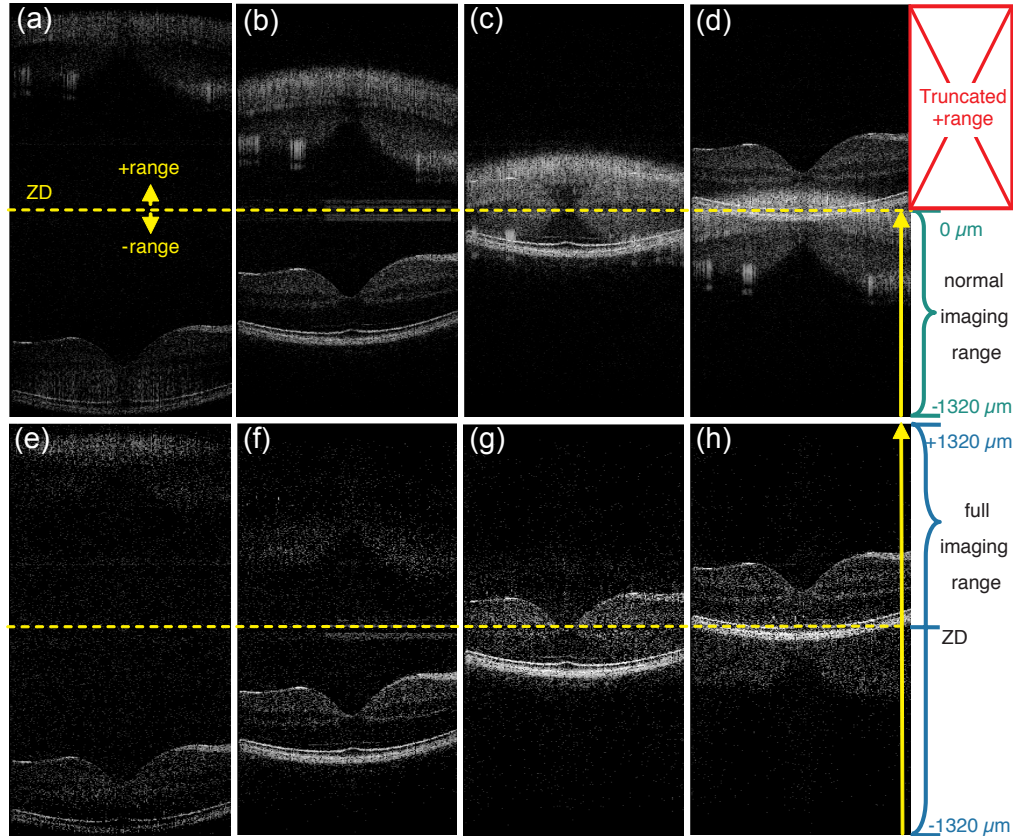


Fig. 5. (a)-(d) Retinal tomograms (fovea) obtained by conventional processing; (e)-(h) tomograms after 256 iterations of dispersion encoded full range (DEFR) algorithm.

Fig. 5(d). The normal imaging range thus is $1320 \mu\text{m}$ and corresponds to the $-$ range. From Fig. 5(c) and (d) it is also visible that structures exceeding the positive end of the $+$ range fold back into the tomogram and cannot be distinguished from the original signal other than they appear blurred due to the numerical dispersion compensation. The artifact suppression resulting from our DEFR scheme can be seen in Fig. 5(e)-(h). After applying the DEFR algorithm with $I = 256$ iterations, the full range tomogram (comprised of $N \times N_x = 2048 \times 1024$ pixels) can be reconstructed, which exhibits twice the depth range compared to conventional processing ($2640 \mu\text{m}$ instead of $1320 \mu\text{m}$). Currently, some artifact components remain visible in the final tomogram, e.g. in the $-$ range of Fig. 5(h). Considering Fig. 5(e), it appears that mirrored aliasing terms affecting Fig. 5(a) around $-1200 \mu\text{m}$ are reduced by DEFR reconstruction.

Figure 6 shows a more detailed view of the full range tomograms with structures imaged around the zero delay position. At this position the complex conjugate artifacts are most disturbing after conventional processing (see Fig. 6(a)). The tomogram resulting with the DEFR algorithm (shown in Fig. 6(b)) exhibits strongly reduced artifacts. Better suppression can be achieved by incorporating additional prior knowledge into the DEFR algorithm. The improved DEFR algorithm employs a global estimate of the average light source power spectrum [43] which is used for pulse shaping of detected true signal components. More specifically the shape of the spectrum $\hat{\mathbf{h}} \in \mathbb{R}^N$ (with elements \hat{h}_n) is first estimated as the mean square value of the

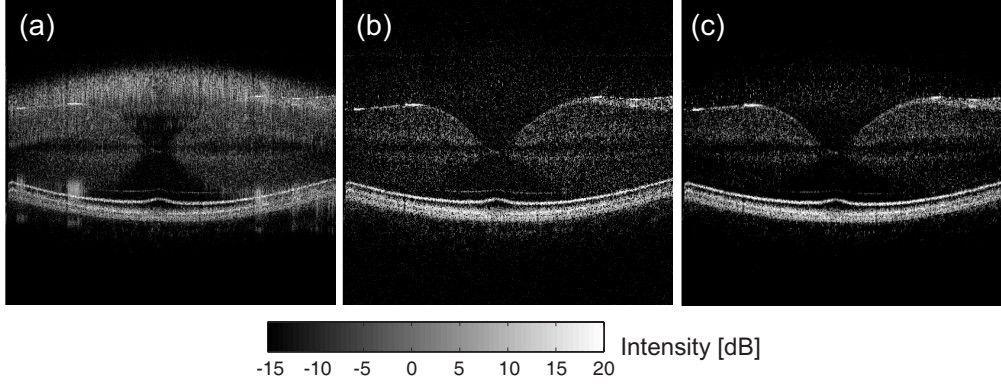


Fig. 6. Tomograms with sample close to zero delay (ZD), (a) conventional processing with dispersion compensation, (b) dispersion encoded full range (DEFER) algorithm, (c) improved DEFER algorithm.

resampled interference spectra $\mathbf{f}_x \in \mathbb{R}^N$ (with elements $f_{x,u}$), i.e.,

$$\hat{h}_u = \sqrt{\frac{1}{N_x} \sum_{x=1}^{N_x} |f_{x,u}|^2}, \quad (24)$$

where x is the spatial index determining the transversal position of an A-scan on the tomogram consisting of $N_x = 1024$ lines and $u = [-\frac{N}{2}, \dots, \frac{N}{2} - 1]$ is the discrete frequency index. Smoothing of $\hat{\mathbf{h}}$ with a zero phase filter and using a Gaussian kernel of length 256 results in $\tilde{\mathbf{h}}$. Finally the normalized pulse spectrum is obtained as

$$\mathbf{h} = \frac{\tilde{\mathbf{h}}}{\|\tilde{\mathbf{h}}\|} \sqrt{N}. \quad (25)$$

For pulse shaping, detected signal components c_{i,n_i} can then be convolved with the inverse Fourier transform of \mathbf{h} . Thereby, the leakage of symmetric terms is further reduced as can be seen in Fig. 6(c). Additional improvement is also expected if the greedy algorithm is evolved to more sophisticated optimization methods. Finally we note that the same intensity range and colorbar has been used for all images. No further image processing steps such as contrast enhancement were applied to the images in Fig. 5 and Fig. 6.

In the presented implementation with results as shown in Fig. 5 one iteration of the algorithm requires 4 times the calculation of a FFT as compared to one FFT for standard processing. Furthermore the total processing time depends on the number of iterations, i.e., the processing time for a single scan line is about $4I$ times more complicated than standard processing (with $I = 256$ processing of a single scan is as costly as standard processing for a tomogram comprised of $N_x = 1024$ A-scans). The asymptotic computational complexity of the algorithm for a single A-scan is about $\mathcal{O}(4IN(1 + \log N))$, whereas standard processing with numeric dispersion compensation obeys $\mathcal{O}(N(1 + \log N))$. A dictionary for the signal components could be used and thereby complexity for one iteration would be in the order of conventional processing. Furthermore multiple non-overlapping components may be detected within each iteration, thus reducing the total number of iterations required. Accordingly neighboring depth-scans could be incorporated to utilize structural similarity. However complexity reduction and speed improvements are beyond the scope of this proof of principle.

5. Conclusion

The iterative dispersion encoded full range (DEFER) algorithm for FD-OCT allows numerical reconstruction of full range tomograms by successive interference cancelation along a single scan line. Whereas existing complex FD-OCT techniques increase the complexity of the measurement setup and require at least two measurements, DEFER needs only one measurement and increases only post-processing complexity. Mirror terms are clearly canceled on retinal tomograms but the algorithm exhibits some leakage on *in vivo* signals with low dynamic range. The quantified artifact suppression ratio of more than 50 dB is promising as it exhibits a value well comparable to the most advanced multiline techniques.

Acknowledgments

The authors thank Cristiano Torti, Alex Tumlinson and Christoph Meier for constructive discussions and two anonymous reviewers for their excellent comments which helped to improve the manuscript. This work was supported in part by Cardiff University; FP6-IST-NMP-2 STREPT (NANOUB - 017128), Action Medical Research (AP1110), DTI OMICRON (1544C), FP7 FunOCT, Grant N10606 of the Austrian Science Fund (NFN SISE), and Carl Zeiss Meditec Inc., Dublin, CA, US.